

3 **Design and Construction of a Cherenkov Detector for**  
4 **Compton Polarimetry at the ILC**5 Christoph Bartels<sup>1,2</sup>, Joachim Ebert<sup>2</sup>, Anthony Hartin<sup>1</sup>,  
6 Christian Helebrant<sup>1</sup>, Daniela Käfer<sup>1</sup>, and Jenny List<sup>1</sup>7 1- Deutsches Elektronen-Synchrotron DESY  
8 Notkestr. 85, 22607 Hamburg, Germany9 2- Universität Hamburg, Institut für Experimentalphysik  
10 Luruper Chaussee 149, 22761 Hamburg, Germany11 **Abstract**12 This paper describes the design and construction of a Cherenkov detector con-  
13 ceived with regard to high energy Compton polarimeters for the International Linear  
14 Collider, where beam diagnostic systems of unprecedented precision must comple-  
15 ment the interaction region detectors to pursue an ambitious physics programme.  
16 Besides the design of a prototype Cherenkov detector, detailed simulation studies  
17 are presented. Results of a first testbeam campaign with the main objective of  
18 validating the simulation in terms of the light distribution inside the channels and  
19 the channel response are presented. Furthermore, a new method for aligning the  
20 detector without the need of dedicated data taking has been developed.

21 Submitted to JINST

# 1 Introduction

The measurement and control of beam parameters to permille level precision will play an important role in the physics programme [1, 2] of the International Linear Collider (ILC). For electroweak processes, the absolute normalisation of expected event rates depends on both, luminosity and polarisation. The luminosity will be measured to a precision of  $10^{-3}$  to  $10^{-4}$ , while for the luminosity weighted polarisation average an accuracy of  $10^{-3}$  seems achievable [3].

While for beam energy and luminosity measurements the ILC's precision goals have already been achieved at previous colliders, polarimetry has to be improved by at least a factor of two compared to the most precise previous measurement of the SLD polarimeter [4].

The polarisation determination at the ILC will combine the measurements of two dedicated Compton polarimeters, located upstream and downstream of the  $e^+e^-$  interaction point, with measurements from the  $e^+e^-$  interactions themselves. While the  $e^+e^-$  data will finally yield the absolute polarisation scale, the polarimeters provide fast measurements which allow to track variations over time and to detect possible correlations with the luminosity or the polarisation of the other beam. Therefore, each polarimeter has to reach a systematic accuracy of at least  $\delta\mathcal{P}/\mathcal{P} = 0.25\%^1$ . Two polarimeters per beam are required in order to measure the polarisation of the beams in collisions. Both polarimeters have been designed for operation at beam energies between 45 GeV and 500 GeV. A detailed description of the polarimeters can be found in [5].

Both polarimeters make use of the polarisation dependence of Compton scattering to ensure a non-destructive measurement of the longitudinal beam polarisation. Circularly polarised laser light is shot under a small angle onto the individual bunches causing typically in the order of  $10^3$  electrons<sup>2</sup> per bunch to undergo Compton scattering. The energy spectrum of these scattered particles depends on the product of laser and beam polarisations, so that the differential rate asymmetry with respect to the laser helicity is directly proportional to the beam polarisation. Since the scattering angle in the laboratory frame is less than  $10\ \mu\text{rad}$ , a magnetic chicane is used to transform the energy spectrum into a spatial distribution which is then measured by Cherenkov detectors.

A Cherenkov detector was chosen for several reasons:

- (i) In combination with the magnetic chicane, it allows to measure the energy spectrum of many electrons arriving simultaneously. With about  $10^3$  Compton interactions per electron bunch, a statistical precision of  $\delta\mathcal{P} = 1\%$  is achieved for each of the about 3000 bunch positions in a train after only 20 trains ( $\hat{=}$  4 seconds). For the average polarisation of all bunch positions, this corresponds to a statistical error below 0.1% after 1 second [5].
- (ii) For relativistic electrons ( $\beta = v/c \approx 1$ ), Cherenkov radiation is independent of the electron energy. Thus, the number of Cherenkov photons will be directly proportional to the number of electrons per detector channel.

---

<sup>1</sup>for typical ILC beam polarisation values of  $\mathcal{P}_{e^-} \geq 80\%$  and  $\mathcal{P}_{e^+} \geq 30\%$  or even  $\geq 60\%$

<sup>2</sup>or positrons in case of the positron beam of the ILC which is equipped analogously.

62 (iii) Typical Cherenkov media like gases or quartz are sufficiently radiation hard to  
 63 withstand the flux of  $10^7$  electrons passing through the detector per second.

64 Developing a Cherenkov detector suitable for achieving the target precision of  $\delta\mathcal{P}/\mathcal{P} =$   
 65  $0.25\%$  demands improvements in various areas of the experimental setup. On the detector  
 66 side, especially the linearity of the detector response, its homogeneity with respect to the  
 67 entrance point of the Compton electrons as well as the detector's alignment to the beam  
 68 axis are important to control. In order to test these and further aspects, a prototype  
 69 detector has been designed, simulated and constructed as described in the chapters 2  
 70 and 3. The prototype has been operated in a testbeam campaign at the ELSA stretcher  
 71 ring in Bonn, with the main objective of validating the simulation in terms of the channel  
 72 acceptance and light distribution inside the channels employing multi-anode photomulti-  
 73 pliers. The results of these studies are presented in chapter 4, including a new method  
 74 for aligning the detector directly from polarimetry data without the need of expensive  
 75 dedicated alignment data taking.

## 76 2 Detector Design and Simulation

77 A conceptual design for the Cherenkov detector envisioned for the ILC polarimeters is  
 78 shown in Figure 1(a). It will consist of staggered 'U-shaped' aluminium channels lining the  
 79 tapered exit window of the beam pipe, similar to the design proposed in [6]. The channels  
 80 are filled with a Cherenkov gas so that relativistic electrons traversing their base emit  
 81 Cherenkov radiation which is reflected upwards in the hind U-leg to the photodetectors.  
 82 A single channel is sketched in Figure 1(b).

83 The wavelength spectrum of Cherenkov radiation is given by:

$$\frac{dN^\gamma}{d\lambda} = 2\pi\alpha \left(1 - \frac{1}{n^2\beta^2}\right) \frac{1}{\lambda^2} \ell, \quad \text{with:} \quad \begin{array}{ll} N^\gamma & : \text{mean number of photons,} \\ \lambda & : \text{wavelength,} \\ \alpha & : \text{fine structure constant,} \\ n & : \text{radiator's refractive index,} \\ \beta & : \text{velocity } (\beta = \frac{v}{c}), \\ \ell & : \text{radiator length} \end{array} \quad (1)$$

84 While the velocity ( $\beta$ ) can be regarded as constant for electron energies relevant at  
 85 the ILC, the refractive index depends on the wavelength, as well as on the tempera-  
 86 ture and the gas pressure. At small wavelengths, the refractive index typically rises like  
 87  $(n-1) = A/[\lambda_0^{-2} - \lambda^{-2}]$ . This behaviour has been measured for  $\text{C}_4\text{F}_{10}$  for the Ring Imaging  
 88 Cherenkov Detector of the DELPHI experiment at LEP [7]. Furthermore,  $n-1$  is propor-  
 89 tional to the number density of molecules for  $n \approx 1$  [8] and thus increases proportionally  
 90 with the inverse temperature and the pressure.

91 To simplify further references, a right-handed coordinate system, as shown in Figure 1,  
 92 will be used throughout the rest of this publication. Assuming the electron beam travels  
 93 in positive  $z$ -direction, the  $y$ -axis points upwards, and the  $x$ -axis to the left when looking  
 94 in the direction of the electron beam.

## 2.1 Requirements and conceptual design

The design of the Cherenkov detectors for the ILC polarimeters is driven by the requirements listed in the following. In most cases, the exact values will depend on the final design of the accelerator, of the magnetic chicane and of the laser system, which is still subject to change. Therefore only indicative numbers are given here.

### Dynamic Range

The detector has to be able to cover a dynamic range from  $\mathcal{O}(1)$  to several hundreds of Compton electrons per channel and bunch crossing. This applies especially to the channels near the Compton edge, where the asymmetry with respect to the laser helicity is largest [5].

### Homogeneous detector response

At the SLD polarimeter, variations of the detector response with respect to the electrons' entry positions lead to a correction on the analyzing power in the order of  $1\% \pm 0.5\%$  [9]. Although part of this effect was due to a preradiator, which is not foreseen to be employed at the ILC, the SLD example shows that the homogeneity of the detector response needs to be considered and should not contribute more than a permille to the total uncertainty budget.

### Alignment

The Compton edge position has to be controlled to  $\mathcal{O}(100 \mu\text{m})$  in order to keep the impact on the analyzing power below 0.1%. Tilts of the detector typically result in changes of the analyzing power in the order of 0.05%/mrad, depending on the considered channel and rotation axis. These numbers are similar to those observed at the SLD polarimeter [9]. At SLD the alignment was monitored regularly in a dedicated operation mode by moving the detector with respect to the beam and interpolated in between these calibration runs. While this approach could be followed at the ILC, it costs expensive accelerator operation time for which no polarisation measurement can be provided. Therefore the development and test of alignment methods which can be performed during polarimetry data taking are among the goals of the prototype presented here.

### Robustness with respect to backgrounds

A gas with a Cherenkov threshold in the MeV-regime should be used to avoid the emission of Cherenkov light from low energetic electrons and muons, e.g. from the beam halo, from beam-gas interactions, or electrons pair-produced from synchrotron radiation. A layout allowing the photodetectors and electronics to be placed well outside the beam-plane is mandatory.

### Detector Linearity & Calibration system

The linearity of the detector response has to be controlled to a level of about 0.75% in order to limit the effect on the analyzing power to 0.1%. Therefore, a dedicated calibration system is foreseen to monitor the detector response, especially its linearity, in-situ. This could be realised by equipping the channels with light emitting diodes (LEDs) which should also be placed outside the beam-plane. Such a system could collect data during breaks in the accelerator operation, or even in-between two ILC bunch trains.

138 The chosen channel geometry is illustrated in Figure 1. The (Compton scattered) elec-  
139 trons traverse the horizontal U-base, while the upward pointing legs serve to place the  
140 photodetectors and the calibration system outside of the beam-plane. With increasing  
141 length of the U-base more Cherenkov light is produced, but on the other hand the align-  
142 ment requirements become more stringent and additional reflections will decrease the light  
143 yield. Simulations suggest that a length of 15 cm is a reasonable choice.

144 In contrast to the ILC-like design of 20 staggered channels (c.f. Figure 1(a)), the prototype  
145 detector consists of two parallel, non-staggered channels. Apart from this difference, the  
146 prototype detector allows to test all relevant aspects of the full detector. Especially it  
147 will serve in the future as a test bed for the calibration system which is currently under  
148 development as well as for the final choice of photodetectors.

## 149 2.2 Optical simulation

150 A detailed simulation of the prototype detector based on GEANT4 [10] has been created  
151 in order to support the design process and the interpretation of the testbeam data.

152 For electrons and positrons Cherenkov radiation, multiple scattering, ionisation, brems-  
153 strahlung and annihilation are simulated. Apart from annihilation, the same processes are  
154 taken into account for muons, which are relevant when studying the impact of accelerator  
155 background. For the Cherenkov photons optical processes have to be considered since  
156 their wavelengths are much larger than a typical atomic spacing. In particular, absorption  
157 in the photodetector entrance window, boundary effects (like reflection and absorption)  
158 at the channel walls, as well as Rayleigh elastic scattering have been included in the  
159 simulation [11].

160 As Cherenkov gas, perfluorobutane ( $C_4F_{10}$ ) has been chosen due to its high threshold of  
161 10 MeV, which makes the detector robust against background from low energetic charged  
162 particles. The wavelength dependence of the refractive index is implemented in the simu-  
163 lation according to [7]. Since the polarisation measurement is based on rate asymmetries,  
164 it will be insensitive to the exact value of  $n$ . Also variations of  $n$  with time which are  
165 slow with respect to the laser helicity flipping rate (like thermal variations) will can-  
166 cel out within the asymmetry. Therefore such effects are currently not simulated and  
167 the temperature and gas pressure inside the detector box are set to  $T = 20^\circ\text{C}$  and  
168  $p = 1\text{ atm} = 1.01325\text{ bar}$ , respectively.

169 Pure  $C_4F_{10}$  is fully transparent even in the far UV range. In the presence of impuri-  
170 ties, especially water or oxygen, the transparency can drop significantly for wavelengths  
171 smaller than 200 nm [12], where two of the four employed photodetectors are sensitive,  
172 c.f. Section 3.1. Since the precise knowledge of the absolute photon yield is not crucial  
173 for the rate asymmetry measurement, gas impurities have not been implemented in the  
174 simulation.

175 Two different types of aluminium have been implemented in the simulation according  
176 to the reflectivity studies summarised in Section 2.5. Three of the four walls of each  
177 channel are made of diamond-milled aluminium, while the inter-channel wall consists

178 of two 150  $\mu\text{m}$  sheets of rolled aluminium. The wavelength dependency is interpolated  
 179 linearly between the values listed in Table 1. While for the diamond-milled walls the  
 180 absolute normalisation is fixed to the values in Table 1, the reflectivity of the rolled sheets  
 181 can be adjusted via the ratio of the two materials' reflectivities  $r := R_{\text{roll}}^{\text{eff}}/R_{\text{diam}}$ , which is  
 182 a parameter of the simulation.

183 Figure 2 shows the channel structure with a single electron (red line) passing from left  
 184 to right through the U-base of the right-hand side channel. It emits Cherenkov light  
 185 (green), which is reflected upwards at the end of the U-base towards the photodetector.  
 186 Cherenkov light produced outside the channel structure in the ambient gas cannot reach  
 187 the photodetectors. The optical simulation ends at the photocathode and all Cherenkov  
 188 spectra are stored for further processing and digitisation.

189 Unless specified otherwise, the simulations shown in the following sections were per-  
 190 formed in view of the testbeam situation at ELSA with a two-dimensional Gaussian with  
 191 standard deviations  $\sigma_x = \sigma_y = 0.5\text{mm}$  as beam profile and zero divergence over the length  
 192 of the detector prototype. Per beam position,  $10^6$  electrons with an energy of 2 GeV have  
 193 been simulated.

## 194 2.3 Cherenkov spectra and light distributions

195 The number of emitted Cherenkov photons follows a Poisson distribution with the mean  
 196 value  $N^\gamma$  given by the integral of Formula 1 over the relevant wavelength range. The  
 197 number of photons reaching the photocathode is expected to follow a Poisson distribution  
 198 as well, as long as other contributions, for instance from electrons showering in the channel  
 199 walls or multiple-scattering in the entrance window, are small.

200 To study the influence of the detector geometry and the reduced reflectivity of the inter-  
 201 channel wall on the expected light distribution, the simulation has been run twice with  
 202 different reflectivities for the inter-channel wall and the beam centered on one of the two  
 203 channels.

204 Figure 3 shows the number of Cherenkov photons reaching the photocathode for both  
 205 cases: In Figure 3(a), all channel walls have been simulated with the reflectivity of  
 206 diamond-milled aluminium, resulting in on average  $N^\gamma = 68$  photons per 2 GeV elec-  
 207 tron. When the reflectivity of the inter-channel wall is reduced to  $r = 50\%$ , about 16%  
 208 less photons reach the photocathode, so that the average decreases to  $N^\gamma = 57$  photons  
 209 as shown in Figure 3(b).

210 In both cases, the distributions of the number of photons reaching the photocathode is not  
 211 exactly Poissonian, but exhibit a small Gaussian broadening due to multiple scattering  
 212 in the entrance window. For illustration, both a pure Poissonian (labeled  $P$ ) as well as a  
 213 Poisson convoluted with a Gaussian (labeled  $P \otimes G$ ) have been fitted to the distributions.  
 214 The respective  $\chi^2$  per degree of freedom values clearly prefer the convoluted fit over the  
 215 pure Poissonian. But with  $\sigma_{\text{Gauss}} \approx 2$  photons, the broadening is small compared to the  
 216 mean number of photons for both reflectivity scenarios and is expected to be negligible  
 217 for the much higher electron energies relevant in the polarisation measurement.



218 Figure 4 shows the wavelength spectrum of these photons obtained from the simulation  
 219 with the reduced reflectivity for the inter-channel wall. Figure 4(a) illustrates the dis-  
 220 tribution at the photocathode, showing the expected  $1/\lambda^2$  wavelength dependence for  
 221 Cherenkov radiation. It is cut off below  $\lambda_{\text{low}} = 160$  nm and above  $\lambda_{\text{high}} = 900$  nm in  
 222 the simulation since the photodetectors are not sensitive outside this wavelength range.  
 223 Figure 4(b) shows the wavelength spectrum after convolution with the quantum efficiency  
 224 of the  $2 \times 2$  multi-anode photodetector (HAMAMATSU R7600U-03-M4). This quantum ef-  
 225 ficiency is shown in the insert in Figure 4(a) [13]. On average, 6.5 photons are detected  
 226 corresponding to the integral of the histogram in Figure 4(b).

227 Figure 5 shows the resulting spatial light distributions on the photocathode, again for two  
 228 different assumptions on the reflectivity of the inter-channel wall. The result obtained  
 229 with equal reflectivities for all inner surfaces is illustrated in Figure 5(a). In this case, the  
 230 observed non-uniformities are due to the influence of the detector geometry. For reference  
 231 a white dot indicates the position of the channel centre. The distribution exhibits an  
 232 X-like structure of increased photon yield which is symmetrical about the  $x$ - and  $z$ -axes.  
 233 A reduced light yield is visible in two narrow bands at  $z = \pm 1$  mm as residuals from  
 234 the  $90^\circ$  reflection at the end of the Cherenkov section. Lowering the reflectivity of the  
 235 inter-channel wall (located at  $x = -4.25$  mm) changes the symmetry of the light pattern  
 236 as shown in Figure 5(b). Near the inter-channel wall, the light yield is reduced, but the  
 237 X-like structure remains.

238 These features can be understood with the sketches in Figure 6, which illustrate two cases  
 239 of photocathode illumination for an electron traversing the channel along its central axis  
 240 and assuming the Cherenkov angle of the chosen gas ( $\Theta_{\text{Ch}} = 3^\circ$ ). Photons emitted in the  
 241 horizontal (or vertical) plane illuminate the entire width of the channel at the photocat-  
 242 ode as shown in Figure 6(a). Due to the larger effective channel cross section, photons  
 243 emitted towards the corners illuminate only half the channel width at the photocathode  
 244 as illustrated in Figure 6(b). This leads to a higher photon yield near the diagonals of  
 245 the channel cross section which also explains the X-like structure observed in Figure 5.  
 246 In addition, Figure 6(b) explains the fact that the lower reflectivity of the inter-channel  
 247 wall leads to a depletion on the same side of the channel.

## 248 2.4 Yield asymmetries and beam position

249 The light distribution on the photocathode has been simulated for a grid scan of  $4 \times 4$   
 250 beam positions with  $10^5$  electrons per position, assuming equal reflectivities for all channel  
 251 walls. Figure 7(a) depicts the light yield on the photocathode for electrons entering the  
 252 Cherenkov section at a fixed  $y$ -position and four different  $x$ -positions. The  $y$ -position of  
 253 the beam, indicated by the white dots in Figure 7(a), translates directly to the  $z$ -position  
 254 in the readout plane of the photodetector. A clear correlation between the light pattern  
 255 and the beam position can be observed in these simulations. If this correlation persists  
 256 in real data, it could potentially be a very useful tool both in a testbeam experiment for  
 257 tuning the simulation and studying the detector properties in detail, as well as in the  
 258 final polarimeter for monitoring the alignment and the Compton edge position during  
 259 data-taking without the need for expensive dedicated calibration beam time.

260 In order to pursue this idea further, the light pattern is quantified in terms of the asym-  
 261 metries in Figures 7(b,c), which are calculated from the light intensities for scans in the  
 262  $x$ - and  $z$ -directions, respectively. For each beam position the corresponding asymmetries  
 263 are defined as

$$A_x = \frac{I_x^+ - I_x^-}{I_x^+ + I_x^-} \quad \text{and} \quad A_z = \frac{I_z^+ - I_z^-}{I_z^+ + I_z^-},$$

264 where  $I_x^+$  ( $I_z^+$ ) corresponds to the intensity in the right (upper) half of a channel and  $I_x^-$   
 265 ( $I_z^-$ ) to the intensity in the left (lower) half, respectively.

266 These asymmetries have an approximately linear dependence on the beam position.

267 Figure 7(b) shows a slight variation of the slope of  $A_x$  depending on the  $y$  position of the  
 268 beam, while in Figure 7(c) the same  $A_z$  is observed for all  $x$  positions. This behavior is  
 269 expected since the active length of the channels increases with  $y$  due to the  $45^\circ$  angle of  
 270 the mirrors.

## 271 2.5 Reflectivity measurements

272 When choosing the detector materials, different qualities of aluminium have been con-  
 273 sidered, primarily with regard to their reflectivity, but also concerning smoothness and  
 274 mechanical stability.

275 Reflectivity measurements of small aluminium probes (blocks, sheets, and sub mm-foils)  
 276 of different quality have been performed with a modified transmission spectrometer [14].  
 277 The path of the measurement beam inside the spectrometer has been changed such that  
 278 it reflects off four small blocks instead of passing through the probe material, as shown  
 279 in Figure 8(a). One photomultiplier detects the previously splitted reference and mea-  
 280 surement beams and thus provides a measure of how much light is reflected by the four  
 281 blocks' surfaces with respect to the reference beam.

282 Figure 8(b) shows measurements of the reflectivity as a function of the wavelength between  
 283  $\lambda = 160$  nm and 600 nm for diamond-milled aluminium blocks and for a sample of rolled  
 284 aluminium foil purchased from GOODFELLOW<sup>3</sup>. In both cases the reflectivity rises at low  
 285 wavelengths up to  $\lambda \approx 250$  nm and is approximately constant at larger wavelengths. For  
 286 the diamond-milled blocks, the reflectivity reaches  $R_{\text{diam}} \approx 85\%$  in the plateau region,  
 287 which is in good agreement with [15]. This material is employed for the mirrors at the ends  
 288 of the U-base, where the reflection occurs approximately under  $45^\circ$  as in the spectrometer.  
 289 Therefore these measured values have been implemented in the simulation.

290 In case of the rolled foil, the measured plateau value of  $R_{\text{roll}} \approx 40\%$  is low, but still in the  
 291 range of reflectivities observed for not perfectly smooth surfaces [15]. However it is not  
 292 directly applicable to the situation in the prototype for several reasons: To start with, the

---

<sup>3</sup>GOODFELLOW GmbH, Germany; Aluminium foil: AL000601 (thickness: 0.15 mm, purity: 99.0%, hardness: hard)



293 reflections on the channel walls occur predominantly under shallow angles ( $\Theta_{\text{Ch}} = 3^\circ$ ).  
 294 Furthermore, any light not following the path expected for an ideal reflector, be it due to  
 295 a finite size of the specular reflection highlight or due to a diffuse reflection component,  
 296 will lead to an immediate intensity loss in the spectrometer, while it still has a high  
 297 probability to reach the photodetector at end of the channel in the prototype. Therefore  
 298 the absolute scale of the spectrometer measurements is considered as a lower limit for the  
 299 effective reflectivity of the inter-channel wall. The wavelength dependency observed in  
 300 the spectrometer measurements is taken into account in the simulation, but the overall  
 301 ratio  $r = R_{\text{roll}}^{\text{eff}}/R_{\text{diam}}$  is a parameter which is varied between 50% and 100% as extreme  
 302 cases, and which ultimately needs to be determined from prototype data. In particular, it  
 303 can be determined from the detector response as function of the beam position if enough  
 304 position scans with sufficient beam quality are available. This is illustrated in Figure 9(a),  
 305 where simulated beam position scans for different values for  $r$  exhibit different slopes of  
 306 the plateau region towards the inter-channel wall. Figure 9(b) shows measurements of this  
 307 slope for both detector channels. The different absolute values of the slopes observed for  
 308 the left and right channel are due to residual misalignment (c.f. Section 4.3). Comparisons  
 309 with a simulation including the misalignment suggest a realistic value of  $r$  of approximately  
 310 85%, which was used in further simulations.

### 311 **3 Construction of the Prototype**

312 The channel dimensions of the prototype were chosen to match the design criteria dis-  
 313 cussed in section 2.1. The length of the U-base relevant for the emission of Cherenkov  
 314 radiation from traversing electrons is 150 mm and the height of the two U-legs is 100 mm.  
 315 A quadratic cross section of  $8.5 \times 8.5 \text{ mm}^2$  has been chosen to match the cathode geom-  
 316 etry of two square multi-anode photomultipliers. Section 3.1 gives further details of the  
 317 employed photodetectors and their characteristics.

318 The size of the outer box is  $230 \times 90 \times 150 \text{ mm}^3$  (L×W×H) allowing for easy accomodation  
 319 of the channel structure. Parts of the technical drawing, e.g. the channel structure and  
 320 its placement inside the box, are shown in Figure 10.

321 Perfluorobutane was chosen as Cherenkov gas due to its high Cherenkov threshold of  
 322 about 10 MeV for electrons. In addition it is neither flammable, nor explosive, contrary  
 323 to propane or isobutane. The 10 mm thick aluminium lid of the box holds an electronic  
 324 pressure gauge suited for remote read-out. The entrance and exit windows for the electron  
 325 beam consist of 0.5 mm thin aluminium sheets.

326 All mountings for LEDs, photodetectors and windows have been designed to be gas- and  
 327 light-tight, as well as easily exchangeable.

#### 328 **3.1 Photodetectors and their mountings**

329 The hind U-leg can be equipped with four different types of photodetectors, which are  
 330 listed in Table 2 along with some of their characteristics. They differ in geometry (square

331 versus round) and the number of anode pads as illustrated in Figure 11. Their gains  
332 are in the order of  $10^6$  with wavelength thresholds between 160 nm and 300 nm and their  
333 response times range from 6.5ns to 28ns. In case of the square multi-anode photodetectors  
334 (MAPMs), one quadrant of their cathodes exactly matches one detector channel. Thus,  
335 both detector channels can be read out simultaneously by the same photodetector.

336 While the round single-anode photodetectors (SAPMs) are inserted into their respec-  
337 tive mountings using appropriate O-ring seals, the MAPMs need to be glued into their  
338 mountings. Epoxy resin mixed with black paint was used as glue to ensure gas- and also  
339 light-tightness. The mountings themselves were manufactured from poly-oxy-methylene  
340 (POM) for electrical insulation. They provide for three different photodetector positions  
341 relative to the detector channels as depicted in Figure 12. In addition, both MAPM  
342 mountings can be rotated by  $180^\circ$  for systematic studies.

### 343 **3.2 LED calibration system**

344 The front U-leg of the detector serves for calibration purposes and is equipped with one  
345 LED per channel. The LEDs have a peak wavelength of 470 nm (HLMP-CB30-NRG,  
346 Agilent Technologies [16]) and are glued into their mounting structure using epoxy resin.

347 As shown in Figure 13, two slender 18 mm long POM tubes encase the LEDs to ensure  
348 that the light from one LED does not enter the neighbouring channel through a small slit  
349 in the inter-channel wall necessary for gas circulation. A temperature sensor is placed in  
350 between the two POM tubes to allow for temperature monitoring.

351 The LEDs and the temperature sensor are fixed in a mounting which has been designed  
352 to be easily exchangeable, because the prototype will serve in the future as a test bed for  
353 a suitable calibration system which is currently under development.

### 354 **3.3 Additional components**

355 Two small, light-tight boxes protect the MAPMs and their electrical bases. A rotation  
356 mechanism on a plastic base plate allows to adjust the detector's horizontal tilt about the  
357  $y$ -axis in reproducible steps of  $0.125^\circ$  between  $\alpha_y = \pm 3.0^\circ$ . The fixed rotational axis lies  
358 in the center of the front U-leg as illustrated in Figure 10(b).

## 359 **4 Beam Tests at the ELSA Accelerator**

360 Beam tests with the prototype detector were performed in an external beam line at ELSA.  
361 The ELEktronen-Stretcher-Anlage (ELSA) is an electron accelerator consisting of three  
362 stages: injector LINACs, a booster synchrotron and the stretcher ring [17]. A beam of  
363 polarised or unpolarised electrons of variable energy up to 3.5 GeV can be stored and used  
364 for various experiments in different beam line areas around the storage ring. The stretcher  
365 ring has a circumference of 164.4 m corresponding to a time of 548 ns for one revolution.  
366 The ELSA beam is structured by the RF frequency of 500 MHz. Of 274 buckets in total,  
367 a variable fraction can be filled. As an example, Figure 14 shows the fill structure for four  
368 revolutions of 548 ns for a partially filled ELSA accelerator.

## 4.1 Setup and pedestal stability

During the testbeam period, ELSA was operated in *booster mode* with the electrons being injected at an energy of 1.2 GeV and subsequently accelerated to 2.0 GeV. The machine cycle is 5.1 s with an extraction time of 4.0 s and the beam can be focussed to a spot size of about 1 mm. The extraction current is adjustable from approximately 10 pA to 200 pA leading to respectively 35 to 700 electrons traversing the detector per ELSA revolution. In comparison, up to 250 electrons per bunch crossing are expected in the most populated channel of a polarimeter Cherenkov detector at the ILC.

The beam clock signal was used to provide the gate for the QDC (charge sensitive analog-to-digital converter), as illustrated in the block diagram of the readout chain in Figure 15. The gate width was adjusted between 100 ns and 480 ns to integrate over the filled part of one ELSA revolution.

The detector was filled with the Cherenkov gas  $C_4F_{10}$  at a slight overpressure of about 140 mbar. This overpressure remained stable although frequent changes to the setup prevented a monitoring of the gas pressure for continuous time periods longer than two weeks. Figure 16 shows the Cherenkov detector set up in one of the ELSA external beam lines, directly behind a dipole magnet bending the electrons by  $\approx 7.5^\circ$  towards a downstream beam dump. The detector was mounted on its base plate (black) and additionally affixed to a stage moveable along the  $x$ - and  $y$ -axis. The two angles,  $\alpha_x$  and  $\alpha_z$ , had to be adjusted using a water-level.

The filled grey histogram in Figure 17(a) depicts the QDC response with no bias voltage applied to the photodetector (pedestal) and without ELSA operation, while the open histograms show the QDC response for a bias voltage of 400V applied to the photodetector (dark current). The dark (light) colour corresponds to the case without (with) beam circulating in ELSA. All three histograms are normalised to the same number of entries. Both, the photodetector dark current and the accelerator operation, lead to a slight broadening of the pedestal peak, but its position remains stable. This is illustrated further by Figure 17(b) which shows again a dark current signal (filled grey histogram) recorded while beam was circulating in ELSA, and, in addition, Cherenkov signals for three different extraction currents (open coloured histograms). Besides the beam signals, each open histogram features a small peak coinciding with the pedestal position because the data taking continued during the 1.1 s of filling and acceleration. This provides the opportunity to monitor the pedestal stability continuously during beam operation. The relative areas of beam signal and pedestal peaks reflect the 4:1 ratio defined by the 5.1 s-periodic cycle of extraction and refill/acceleration times. Longterm monitoring showed that the pedestal position remained stable within 1 QDC count, which fulfills the ILC requirements. All following Figures show pedestal-subtracted signals.

## 4.2 Online alignment and channel response function

The alignment of the detector with respect to the electron beam line was obtained from beam data. By moving the detector stage, the incident beam position on the entrance

409 window was scanned in horizontal ( $x$ ) and vertical ( $y$ ) directions. The adjustment proce-  
 410 dure requires one vertical scan for each detector channel and a series of horizontal scans  
 411 across both channels for different tilt angles  $\alpha_y$ , as shown in Figure 18.

412 When the detector is tilted, the electrons will not have the full channel length to produce  
 413 Cherenkov light. The maximal signal for any given  $x$  position of the beam will be smaller  
 414 than for a perfectly aligned detector <sup>4</sup>. For each tilt angle, the beam  $x$  position resulting  
 415 in the highest signal is determined as displayed in Figure 18. With this procedure, the  
 416 best alignment of the detector with respect to the beam line was obtained for a tilt angle  
 417 of  $\alpha_y = 1.33^\circ$  with a very small statistical uncertainty of  $0.03^\circ$ . Due to the step size  
 418 of the rotation mechanism, this value was approximated to  $\alpha_y^0 = 1.35^\circ$  for all following  
 419 measurements.

420 Measurements of the detector response as function of the horizontal beam entry position  
 421 were performed with the single-anode photomultiplier R7400U-06 and with the 2×2 multi-  
 422 anode photomultiplier (R7600U-03-M4) positioned on the detector channels as illustrated  
 423 in Figure 12(c). Figure 19(a) shows for the latter case the results of an  $x$ -scan across  
 424 both detector channels. Two Gaussian fits indicate the respective channel centres to  
 425 be at  $x_{\text{right}} = (7.4 \pm 0.1)$  mm and  $x_{\text{left}} = (16.4 \pm 0.1)$  mm, leading to a distance of  
 426  $\Delta x = (9.0 \pm 0.2)$  mm. This agrees with the nominal distance between the channel centres  
 427 of  $\Delta x_{\text{nom}} = 8.8$  mm, given by the width of one channel and the inter-channel wall.

428 Figure 19(b) shows  $x$ -scan data for the single-anode photomultiplier, where a broad  
 429 plateau is observed. The width of the signal region is determined from two sigmoidal  
 430 fits to the edges of the plateau. At 50% of the plateau height, this width is found to  
 431 be  $w = (9.4 \pm 0.3)$  mm, where the error is dominated by the table position accuracy.  
 432 This value is significantly larger than expected from the physical channel width and from  
 433 Monte–Carlo simulations. Understanding the channel response function to the precision  
 434 level required for the ILC will need further data with more stable beam conditions than  
 435 available from the 2009 campaign.

436 The impact of the beam conditions becomes evident by comparing the observed channel  
 437 reponse functions from 19 with the corresponding photographs of a fluorescent screen  
 438 placed on the detector entrance window: Figure 20(a) shows a very elongated beam spot  
 439 observed at the time the MAPM data were recorded (Fig. 19(a)), which explains the  
 440 absence of any plateau in the detector response. The significantly smaller and nearly  
 441 round beam spot shown in Figure 20(b) was achieved during data taking with the SAPM  
 442 (Fig. 19(b)).

### 443 4.3 Alignment via spatial asymmetries

444 The anode of the 8×8 multi-anode photomultiplier (R7600-00-M64) is finely segmented  
 445 with 16 anode pads covering a single Cherenkov channel, thus offering spatial resolution  
 446 within a detector channel. Since two QDC channels were broken, only six channels were

---

<sup>4</sup>Due to the channel geometry, this holds for all tilt angles larger than  $0.027^\circ$ .

447 available to realise the readout configuration illustrated in Figure 21. The numbers indi-  
 448 cate the QDC channel utilised to read out the sum signal of either four or eight anode  
 449 pads of the photodetector.

450 Figure 22 shows the results of (a) an  $x$ -scan across both detector channels and (b) the  
 451 corresponding  $y$ -scan across the left channel. As expected, the signals in QDC channels 2  
 452 and 3 are about twice as large as in the other channels since eight instead of only four  
 453 anode pads are grouped together. The asymmetric response reflects the incident beam  
 454 position. For each QDC channel, the largest signal is observed when the beam enters on  
 455 the opposite side of the detector channel. This confirms the prediction of one glancing  
 456 angle reflection for most of the photons obtained from MC simulations (c.f. Section 2.3  
 457 and 2.4).

458 For a more detailed comparison of the responses of the different anode segments, the same  
 459 data are displayed again in Figure 23, scaled and mirrored to correct for the two above  
 460 effects. Possible reasons for the remaining shape and amplitude differences comprise gain  
 461 variations between the pads and residual detector misalignment.

462 The vertical beam scan data have been used to calibrate the relative gain variations  
 463 between the different groups of anodes. After applying these calibrations to the horizontal  
 464 beam scans, two  $x$ -asymmetries,  $A_x^{lower}$  and  $A_x^{upper}$ , are calculated from the four anode  
 465 groups QDC 4 to QDC 7 (c.f. Figure 21):

$$A_x^{lower} = \frac{\text{QDC 5} - \text{QDC 4}}{\text{QDC 5} + \text{QDC 4}} \qquad A_x^{upper} = \frac{\text{QDC 6} - \text{QDC 7}}{\text{QDC 6} + \text{QDC 7}}$$

466 The resulting asymmetries are displayed in Figure 24(a), together with the expectation  
 467 from simulation assuming residual tilts of  $\alpha_x = 0.2^\circ$  and  $\alpha_y = -0.2^\circ$  and a reflectivity ratio  
 468 of  $r = 85\%$ . The error bars on the data points correspond to the remaining gain differences  
 469 between the anode pads. Uncertainties which are in common between the different pads  
 470 cancel out within the asymmetries. The error bands on the simulated curves are obtained  
 471 by varying  $\alpha_y$  by  $\pm 0.1^\circ$  in the simulation. A similar variation of  $\alpha_x$  has no visible impact  
 472 on  $A_x$ . Figure 24(b) shows  $A_x^{lower}$  and  $A_x^{upper}$  for the other detector channel, read-out  
 473 by the neighboring quadrant of the  $8 \times 8$  MAPM<sup>5</sup>, compared to the simulation using  
 474 exactly the same parameters as before. The obtained precision of  $\pm 0.1^\circ$  is very close to  
 475 the requirements for the ILC, which shows that in principle the light distribution inside  
 476 a channel can be understood to sufficient precision. But due to the extremely limited  
 477 number of datasets with good beam conditions (c.f. Section 4.2) no further independent  
 478 beam scan is available from the 2009 data-taking period at ELSA. Therefore further data-  
 479 taking will be needed for conclusive statements on the use of multi-anode photodetectors  
 480 in ILC polarimeters.

---

<sup>5</sup>Due to the two broken QDC channels, these data could not be taken simultaneously, but stem from a subsequent run after changing the readout combination of anode segments at the QDC.

## 5 Conclusions

At a future  $e^+e^-$  linear collider, Compton polarimeters will be employed to measure the beam polarisation to a precision of  $\delta\mathcal{P}/\mathcal{P} = 0.25\%$ , using Cherenkov detectors to register the scattered Compton electrons.

A compact two channel prototype detector has been designed and constructed such that it will allow nearly all aspects of the final detector to be studied. In particular, it has been designed for easy exchange of the photodetectors and the calibration light source, but also the inter-channel wall could be exchanged in order to test different materials for a final detector.

The prototype has been operated successfully in a first testbeam campaign using four different photodetectors. The dynamic range of the detector and the pedestal stability fulfill the ILC requirements. The measurements have been compared to a detailed simulation of the prototype and several alignment methods have been tested.

In particular, a method to extract intra-channel beam position information has been developed, which could possibly allow to calibrate the Compton edge position without need for dedicated beam-time. Furthermore, the detector response has been studied as a function of the beam position. This will lead to a determination of each channel's response function which is important in order to control systematic effects on the final polarisation measurements.

In the future it is planned to use this prototype to compare different photodetectors and wall materials as well as to establish a calibration to the permille level as required for the ILC.

## Acknowledgements

We thank C. Hagner and R. Klanner of the Institut für Experimentalphysik of the University of Hamburg for their support, and especially the design and technical construction team, B. Frensche and J. Pelz, as well as the head of the mechanical workshop, S. Fleig, and his entire team for their competent work.

The authors are grateful to W. Hillert, F. Frommberger and the entire ELSA team for their support during the testbeam period, for realising special beam requests and for many helpful discussions concerning a multitude of different ELSA technicalities. Further thanks go to K. Desch, J. Kaminski, D. Elsner, and many others for help and support with the planning and setup before, during, and after the two weeks in Bonn.

The authors acknowledge the financial support of the Deutsche Forschungsgemeinschaft in the DFG project Li 1560/1-1 as well as the complementary support by the Initiative and Networking Fund of the Helmholtz Association, contract HA-101 (“Physics at the Terascale”).



## References

- 517
- 518 [1] The ILC Collaboration, “*ILC Reference Design Report, Volumes 1-4*”  
519 “*1: Executive Summary*,” J. Brau, Y. Okada, N. Walker (eds.) [arXiv:0712.1950 physics.acc-ph];  
520 “*2: Physics at the ILC*,” A. Djouadi, J. Lykken, K. Mönig, Y. Okada, M. Oreglia, S. Yamashita  
521 (eds.) [arXiv:0709.1893 hep-ph];  
522 “*3: Accelerator*,” N. Phinney, N. Toge, N. Walker (eds.) [arXiv:0712.2361 physics.acc-ph];  
523 “*4: Detectors*,” T. Behnke, C. Damerell, J. Jaros, A. Miyamoto (eds.) [arXiv:0712.2356 physics.ins-  
524 det].
- 525 [2] G.A. Moortgat-Pick *et al.*, Phys. Rept. **460** (2008) 131, [arXiv:hep-ph/0507011].
- 526 [3] I. Marchesini, “Triple Gauge Couplings and Polarization at the ILC and Leakage in a Highly Granular  
527 Calorimeter” Ph.D. Thesis, University of Hamburg, Hamburg, Germany, 2011.
- 528 [4] The ALEPH, DELPHI, L3, OPAL and SLD Collaborations, the LEP and SLD Electroweak Working  
529 Groups and the SLD Heavy Flavour Group, Phys. Rept. **427** (2006) 257; [arXiv:hep-ex/0509008].
- 530 [5] S. Boogert *et al.*, JINST **4** (2009) P10015. [arXiv:0904.0122v2 physics.ins-det].
- 531 [6] V. Gharibyan, N. Meyners, and K.P. Schüller, TESLA Report 2001-23, Part III, LC-DET-2001-047,  
532 DESY, February 2001; DESY 2001-011, March 2001
- 533 [7] E. Fokitis *et al.*, Nucl. Phys. Proc. Suppl. **44** (1995) 246,  
534
- 535 [8] A. Bideau-Mehu *et al.*, J. Quant. Spectrosc. Radiat. Transf. **25** (1981), 395.
- 536 [9] R.D. Elia, “*Measurement of the left-right asymmetry in Z boson production by electron-positron*  
537 *collisions*,” SLAC-0429,  
538 R.C. King, “*A precise measurement of the left-right asymmetry of Z boson production at the SLAC*  
539 *linear collider*,” SLAC-0452.
- 540 [10] The GEANT4 Collaboration, Nucl. Instrum. Meth. A **506**, Issue 3 (2003), 250-303;  
541 The GEANT4 Collaboration, IEEE Trans. Nucl. Science 53 No. 1 (2006), 270-278; ISSN: 0018-9499
- 542 [11] The GEANT4 Collaboration, “*GEANT4 – Physics Reference Manual*,”  
543 [http://geant4.web.cern.ch/geant4/UserDocumentation/UsersGuides/PhysicsReference ...](http://geant4.web.cern.ch/geant4/UserDocumentation/UsersGuides/PhysicsReference...)  
544 [Manual/fo/PhysicsReferenceManual.pdf](http://geant4.web.cern.ch/geant4/UserDocumentation/UsersGuides/PhysicsReferenceManual/fo/PhysicsReferenceManual.pdf) (cont’d)
- 545 [12] E. Albrecht *et al.*, “*VUV Absorbing Vapours in n-Perfluorocarbons*,” CERN-EP/2002-099.
- 546 [13] HAMAMATSU PHOTONICS K.K. (<http://sales.hamamatsu.com/> abbrev. as `~hamamatsu/`)  
547 R7600U-03-M4 (2007): `~hamamatsu/assets/pdf/parts_R/R5900U_R7600U_TPMH1291E03.pdf`  
R7600-00-M64 (2006): `~hamamatsu/index.php?id=13195917`  
R7400U-06(03) (2004): `~hamamatsu/assets/pdf/parts_R/R7400U_TPMH1204E07.pdf`
- 548 [14] PerkinElmer, Lambda 800 Spectrometer  
549 <http://las.perkinelmer.com/Catalog/default.htm?CategoryID=Lambda+800+Spectrometer>
- 550 [15] John E. Hatch (Ed.), “*Aluminum: Properties and Physical Metallurgy*,” American Society for Metals,  
551 Metals Park, Ohio, USA, 1984.
- 552 [16] Agilent Technologies, LED of type: HLMP-CB30-NRG00  
553 Datasheet: <http://www.chipcatalog.com/Agilent/HLMP-CB30-NRG00.htm>
- 554 [17] W. Hillert, Eur. Phys. J. A **28S1** (2006) 139.
- 555 [18] PHOTONIS USA  
556 XP1911/UV (1999): <http://www.photonis.com/upload/industryscience/pdf/pmt/XP1911UV.pdf>

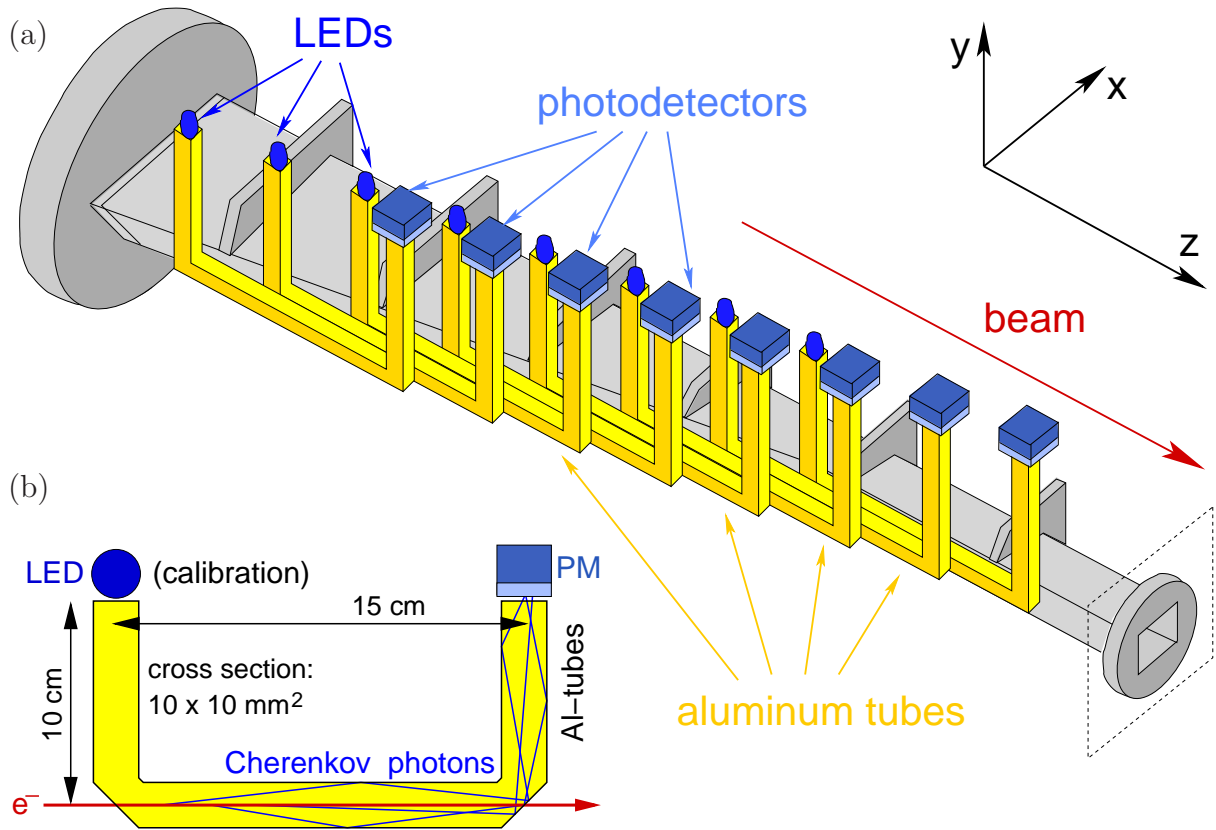
wavelength	$R_{\text{diam}}$	$R_{\text{roll}}$
160 nm	74 %	11 %
180 nm	77 %	18 %
200 nm	81 %	27 %
220 nm	84 %	30 %
240 nm	86 %	37 %
500 nm	85 %	40 %
520 nm	84 %	39 %
650 nm	83 %	40 %
900 nm	82 %	39 %

**Table 1:** The reflectivities of diamond-milled quality aluminium  $R_{\text{diam}}$  and of rolled quality aluminium  $R_{\text{roll}}$  as determined with the PERKINELMER spectrometer and implemented in the GEANT4 simulation. For the rolled aluminium, only the wavelength dependency is transferred to the simulation, while the absolute normalisation is adjusted to prototype data.

photodetector types	sensitive area in [mm <sup>2</sup> ]	wavelength range [nm]	typical gain	response time	anode pads
R7600U-03-M4 <sup>(a)</sup>	18.0 × 18.0	185 - 600	1.8 · 10 <sup>6</sup>	11.0 ns	4
R7600-00-M64 <sup>(a)</sup>	18.1 × 18.1	300 - 600	0.3 · 10 <sup>6</sup>	13.4 ns	64
R7400U-06(03) <sup>(a)</sup>	∅ = 8 mm	160(185) - 600	0.7 · 10 <sup>6</sup>	6.5 ns	1
XP1911/UV <sup>(b)</sup>	∅ = 15 mm	200 - 600	0.9 · 10 <sup>6</sup>	28.0 ns	1

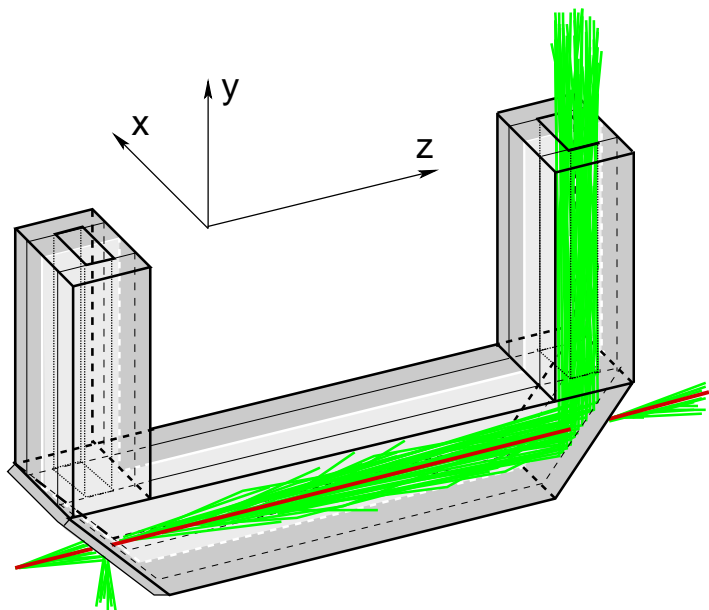
Photodetector from: (a) HAMAMATSU, (b) PHOTONIS.

**Table 2:** Key characteristics of the four different photomultipliers from HAMAMATSU and PHOTONIS [13, 18]. The two MAPMs (R7600U-03-M4 and R7600-00-M64) have a quadratic cross-section of similar size, but differ in the number of anodes and in their wavelength range. The two SAPMs (R7400U-03 and R7400U-06) differ in the size of their sensitive areas and slightly in wavelength range.



**Figure 1:** (a) Illustration of a Cherenkov detector for ILC polarimetry, here for better visibility with eight instead of the actually foreseen 20 readout channels; and (b) sketch of one such gas-filled aluminium channel.

**Figure 2:** Event display of the 2-channel prototype simulation: The electron beam (red) passes from left to right through the U-base of the aluminium tubes filled with perfluorobutane,  $C_4F_{10}$ , and emits Cherenkov photons (green). These are reflected upwards to a photodetector mounted on the hind U-leg. The channels are separated by a thin foil (light grey). Due to a surrounding gas-filled box (not shown), Cherenkov radiation can also be emitted before/after the electron beam enters/exits the aluminium tubes, but it cannot reach the photodetector.



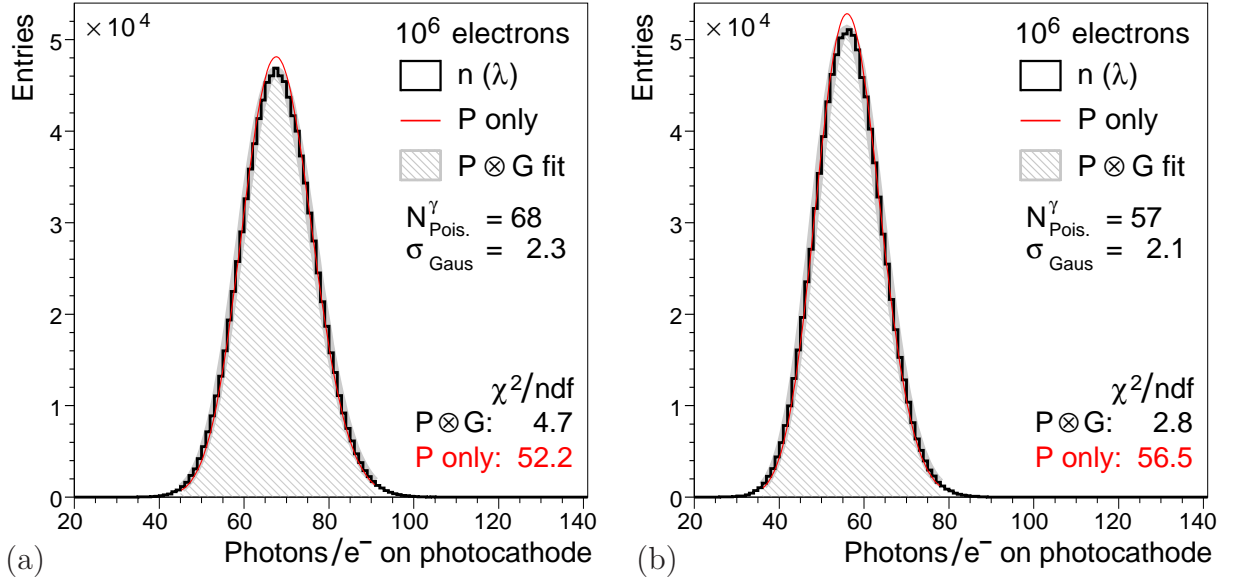


**Figure 3:** Average number of photons reaching the photocathode per 2 GeV electron: (a) with equal reflectivities for all channel walls and (b) with a reduced reflectivity of the inter-channel wall ( $r = 50\%$ ).

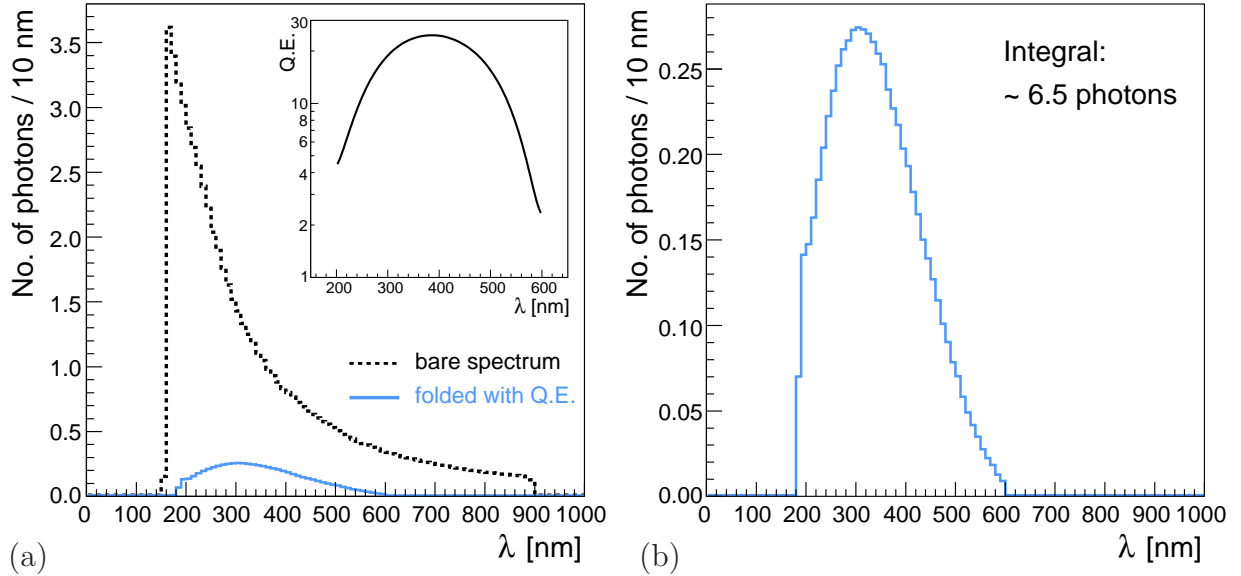


**Figure 4:** Cherenkov spectra: (a) at the photocathode (dotted line) and (b) convoluted with the quantum efficiency (Q.E.) of the  $2 \times 2$  MAPM (R7600U-03-M4), see the insert in (a). The convoluted spectrum is also superimposed in (a) as the solid line.

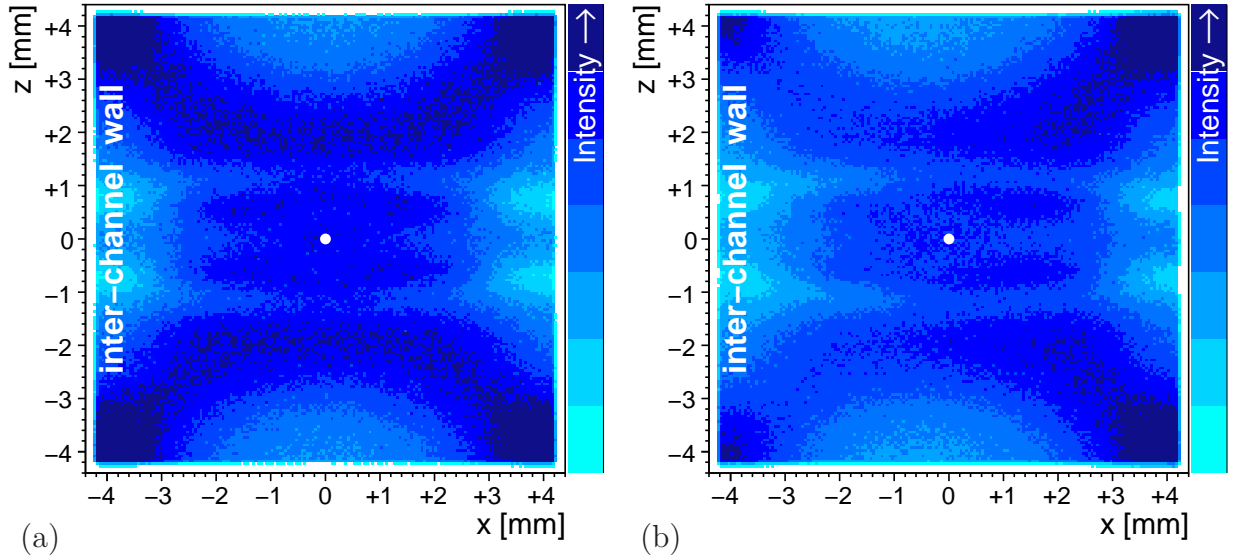
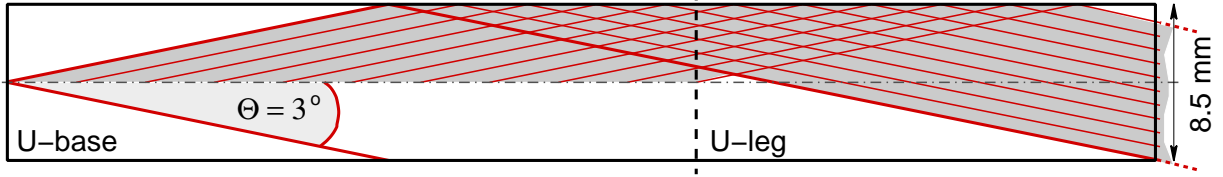


**Figure 5:** Light distribution on the photocathode: (a) with equal reflectivities for all channel walls, (b) with a reduced reflectivity for the inter-channel wall at  $x = -4.25$  mm. The white dot indicates the channel centre; the intensity scale ranges from 40% to 100%.

(a) photons emitted in the horizontal/vertical plane



(b) photons emitted toward the channel corners

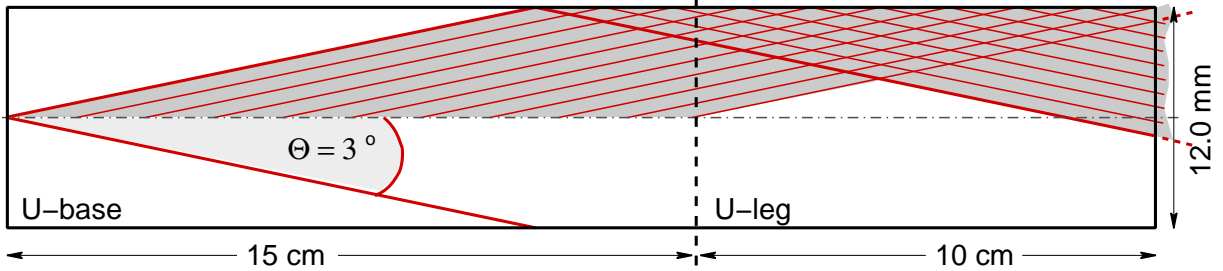


**Figure 6:** Sketches of possible light paths for electrons traversing the channel along the central axis and the Cherenkov angle of the chosen gas ( $\Theta_{\text{Ch}} = 3^\circ$ ). The channel aspect ratio has been enlarged by a factor of 4 for better visibility.

(a) Photons emitted in the horizontal/vertical plane illuminate the entire channel width at the photocathode, while (b) photons emitted towards the channel corners only illuminate half the channel width. The  $90^\circ$  reflection at the end of the U-base (indicated by the vertical dashed line) has no influence on the symmetry of the distribution.

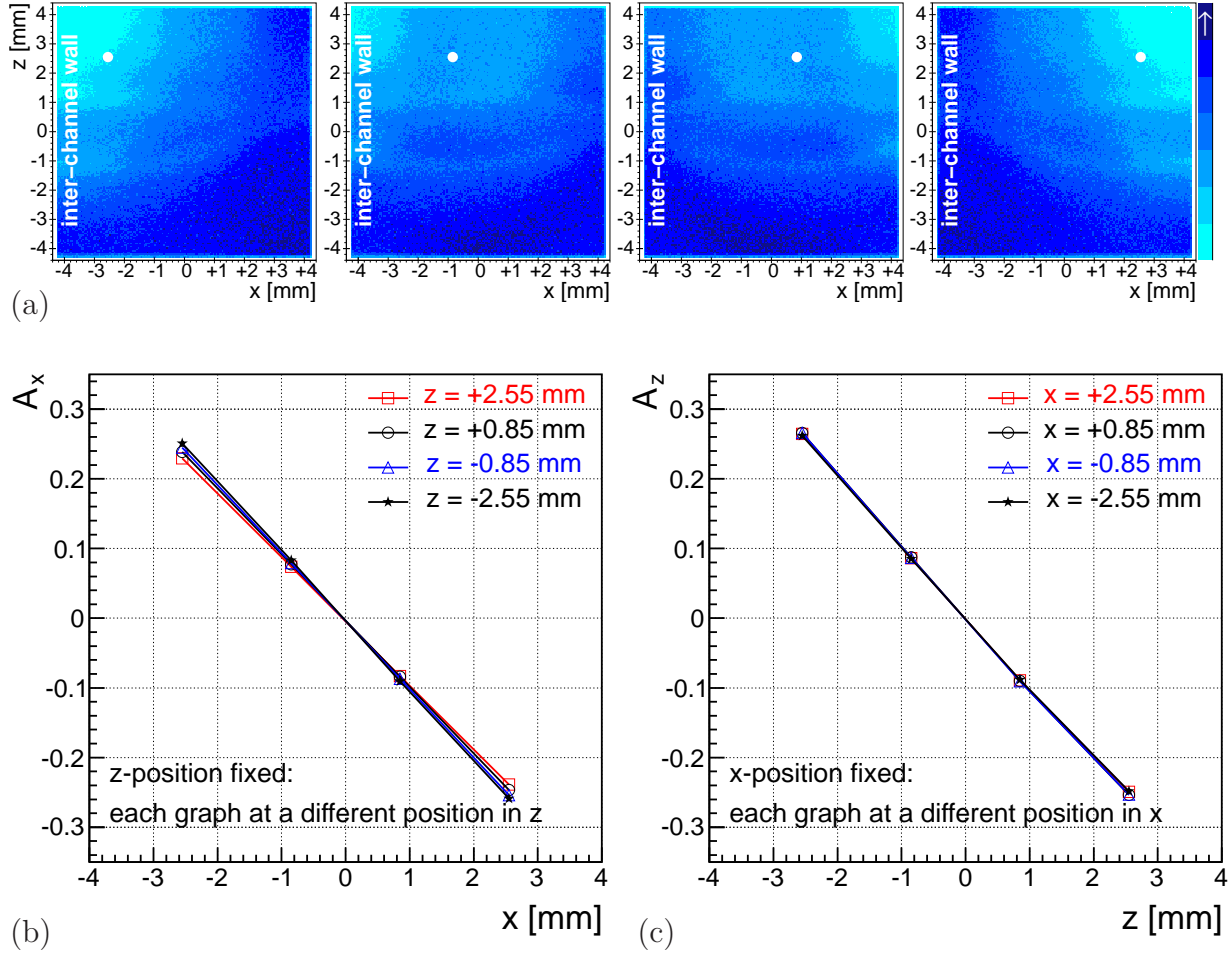


**Figure 7:** (a) Simulated light yield at the photocathode for a horizontal beam position scan at  $y = +2.55$  mm and equal reflectivities for all channel walls. The asymmetries have been calculated respectively from horizontal and vertical scans using  $10^5$  electrons for each beam position: (b)  $A_x$  asymmetry for different  $z$ -positions and (c)  $A_z$  asymmetry for different  $x$ -positions.

The beam  $y$ -position translates directly to the  $z$ -position in the readout plane (white dots).



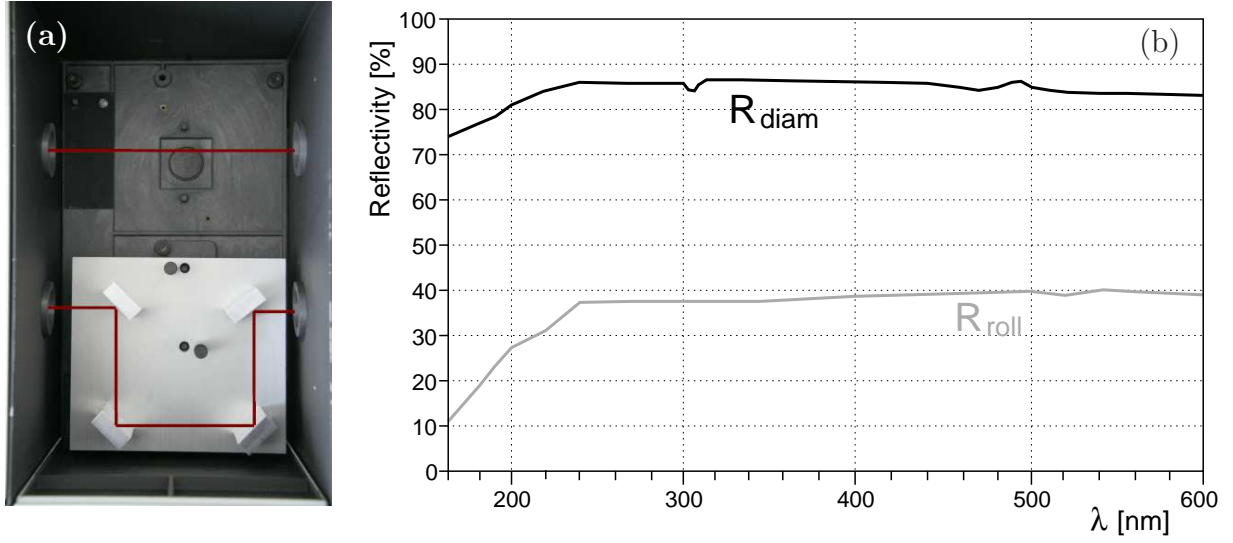


**Figure 8:** (a) Photograph of the interior of the modified PERKINELMER transmission spectrometer with the indicated paths of the reference beam (top) and the measurement beam (bottom). (b) Measured reflectivities of diamond-milled aluminium (upper line) and of rolled aluminium (lower line).

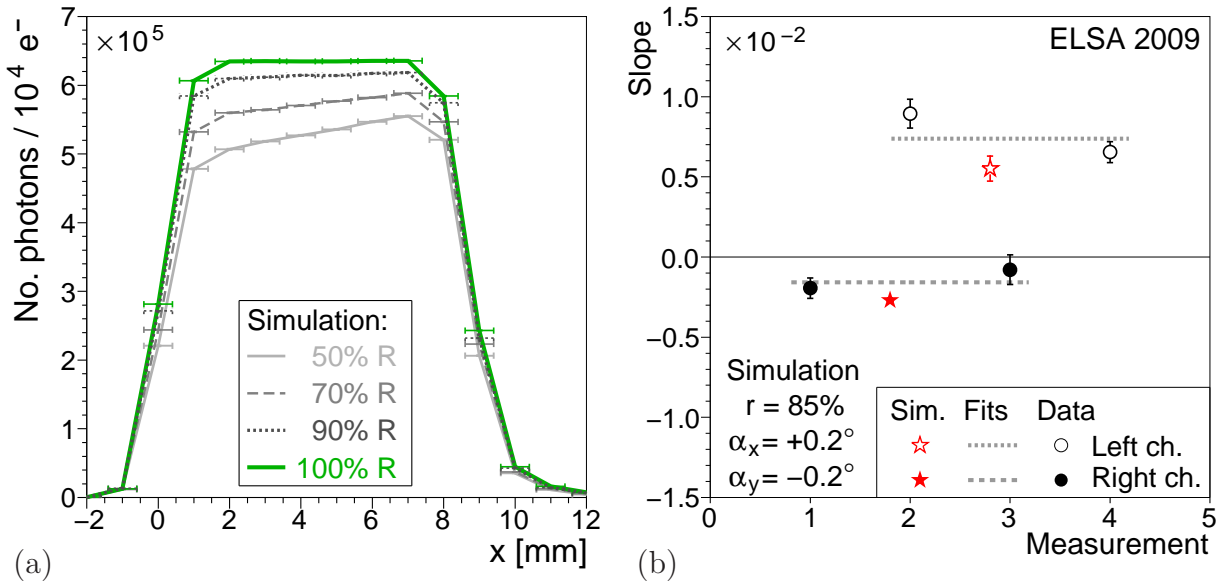


**Figure 9:** (a) Simulations with different percentages of the inter-channel wall reflectivity w.r.t. to the other walls' reflectivities lead to different plateau shapes. (b) A comparison with data allows to determine the inter-channel wall reflectivity to be  $R_{\text{roll}} = (85\% \pm 2\%) \cdot R_{\text{diam}}$  under glancing angle.

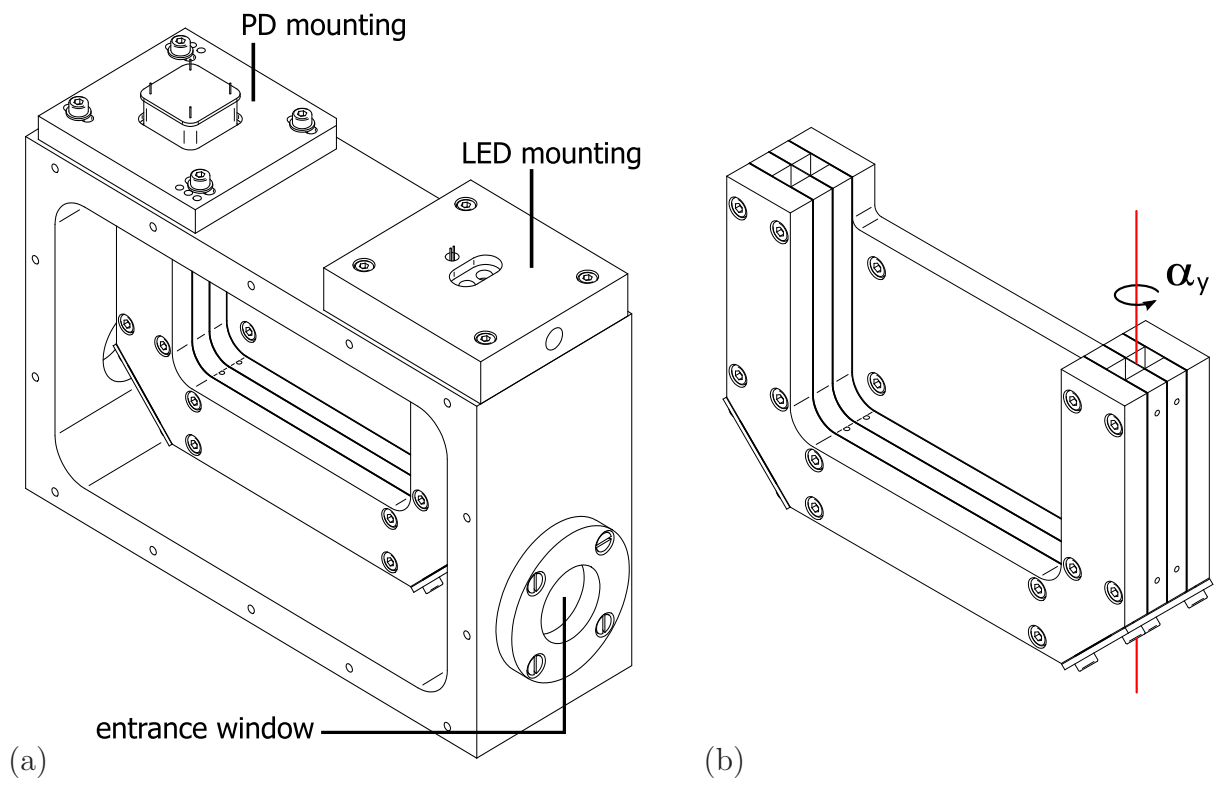


**Figure 10:** Parts of a technical drawing for the assembly of the prototype: (a) the box base body, already including the channel structure (b) of two parallel U-shaped channels.

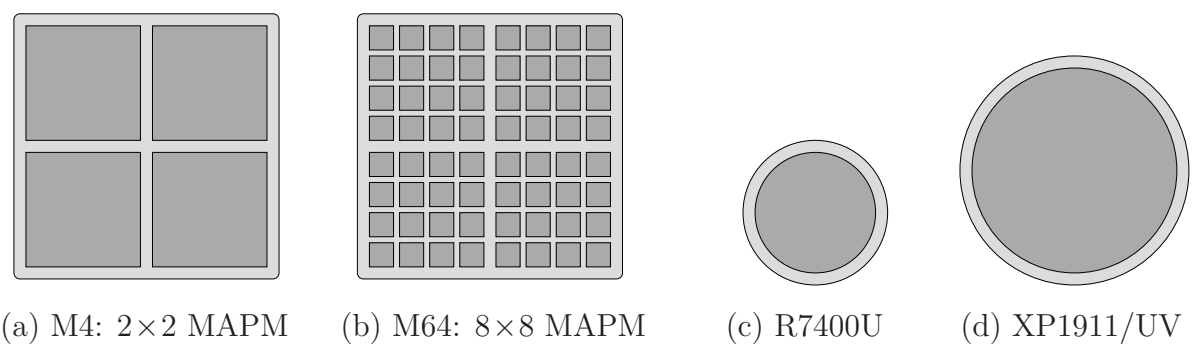


**Figure 11:** Anode schemes of the different multi- and single-anode photomultiplier types, in correct relative scaling.

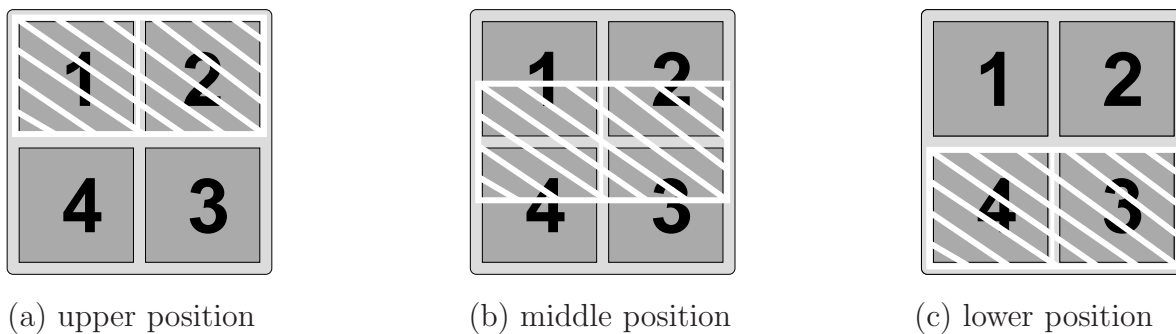


**Figure 12:** Different positions of the MAPMs (grey) on the detector channels (hatched).



**Figure 13:** Calibration LEDs covered by POM tubes.

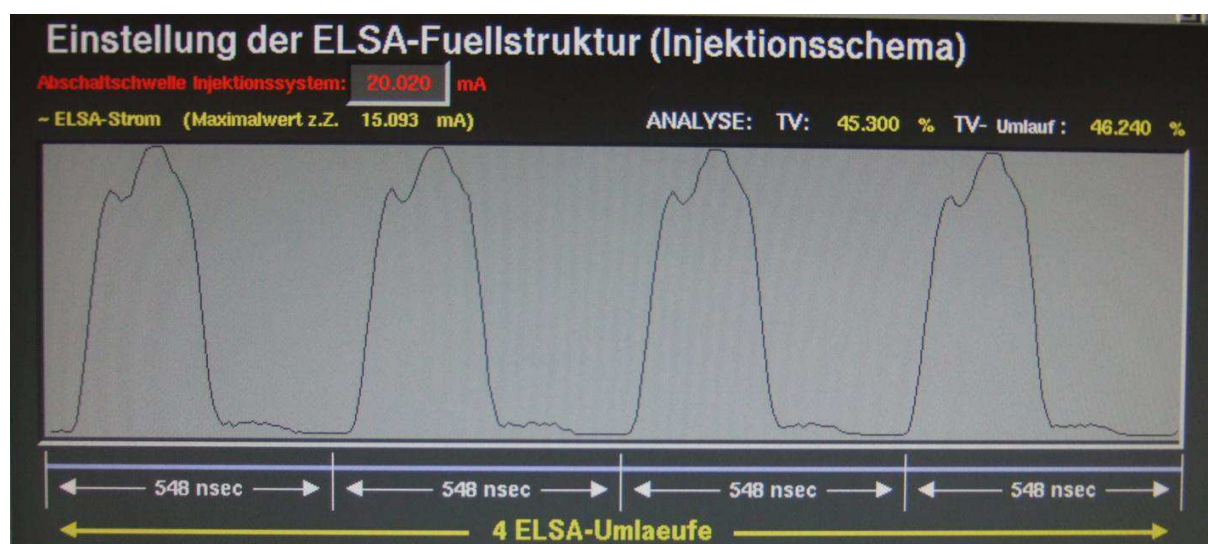


**Figure 14:** Example of a typical ELSA fill structure for four revolutions of 548 ns. About half of the available buckets are filled.

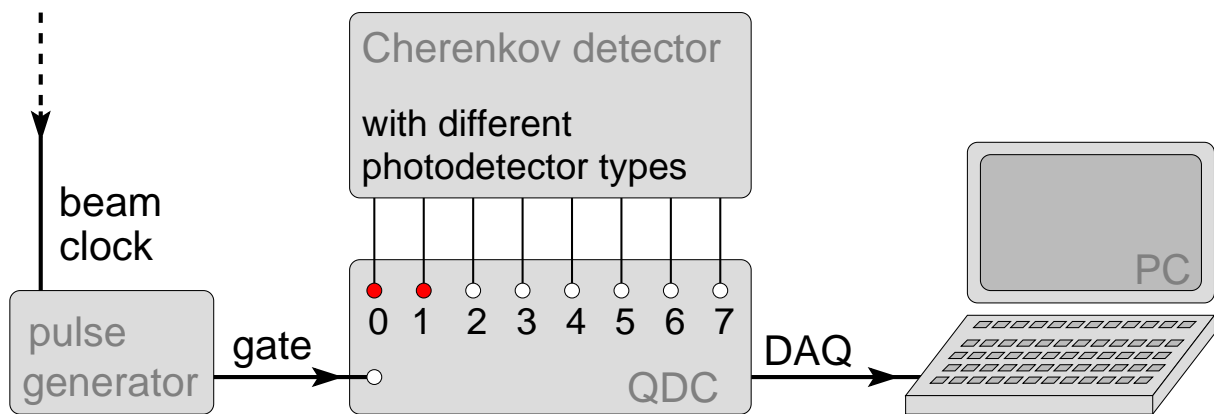


*Figure 15: Block diagram of the readout chain as realised during the testbeam period.*

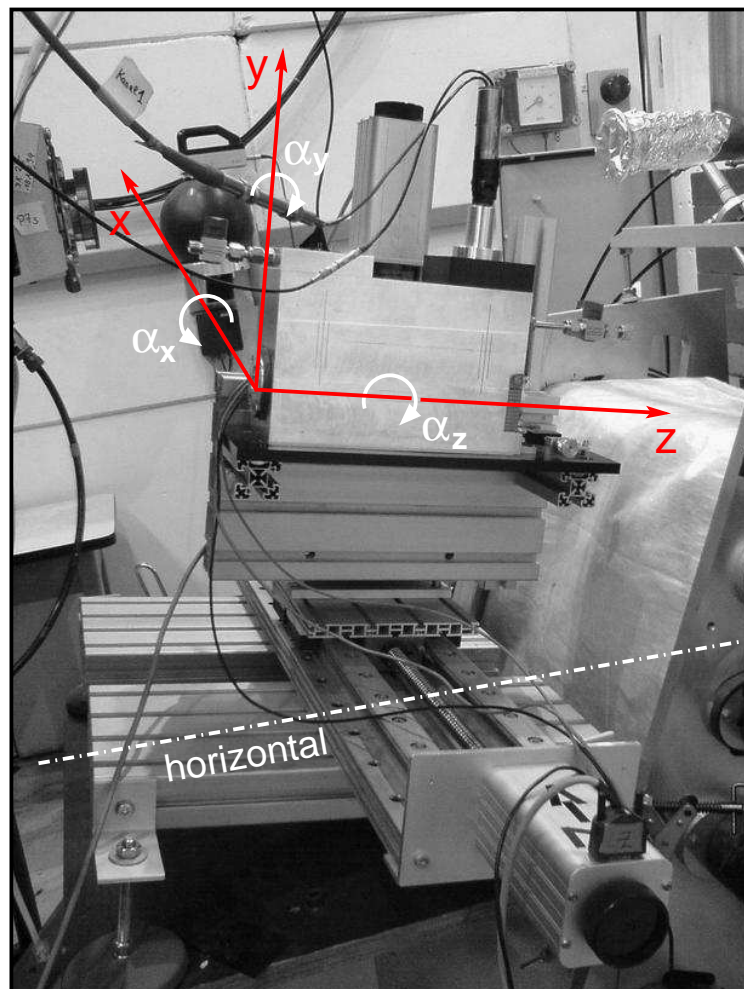


*Figure 16: The prototype Cherenkov detector on its base plate (black, with the rotational mechanism visible on the right) is mounted on a stage moveable along the x- and y-axis.*

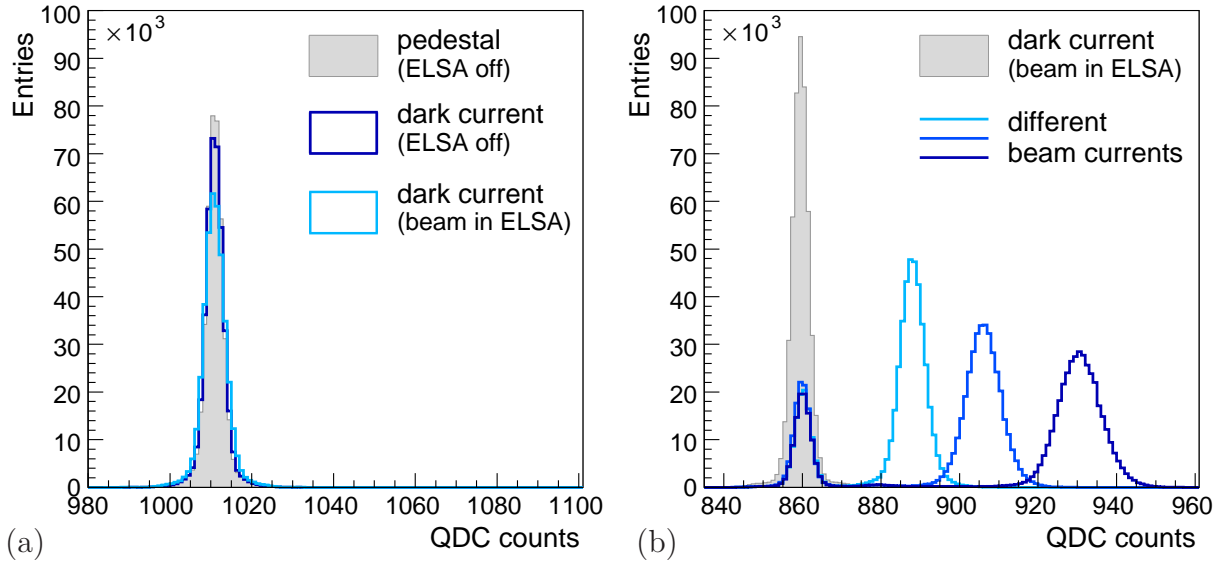


**Figure 17:** Data recorded with the  $2 \times 2$  MAPM (R7600U-03-M4):  
 (a) QDC response without bias voltage applied to the photodetector (pedestal) and with 400 V applied (dark current), both without and with beam circulating in ELSA.  
 (b) Cherenkov signals increase with increasing electron beam current, while the pedestal position remains stable. The 4:1 area ratio between the beam signal peak and the pedestal of each open histogram corresponds to the beam extraction cycle of 4s:1s.

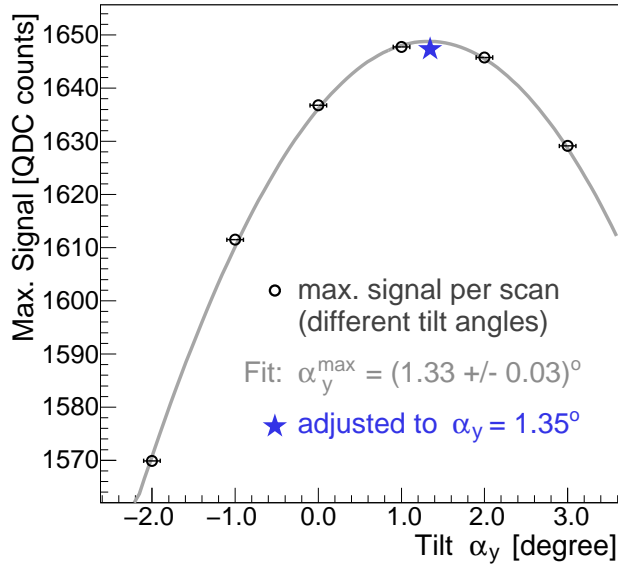


**Figure 18:** Detector alignment with the  $2 \times 2$  MAPM (bias voltage 860 V): The tilt in the  $(x, z)$ -plane is determined from  $x$ -scans for six different tilt angles. An additional measurement for the adjusted tilt of  $\alpha_y = 1.35^\circ$  is also displayed.

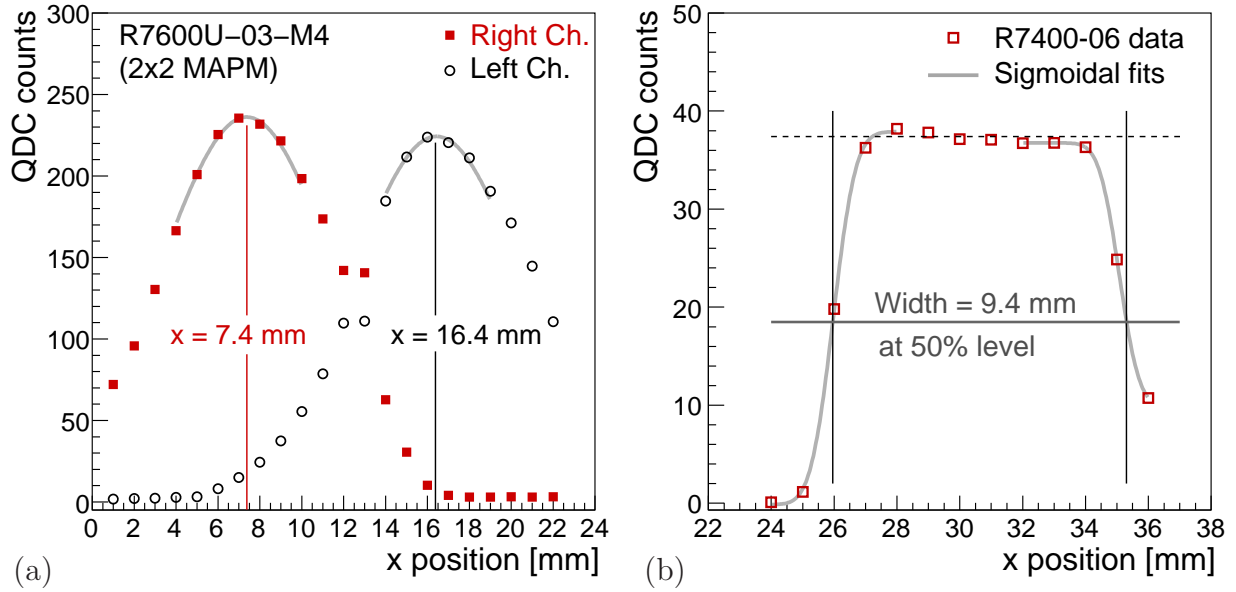
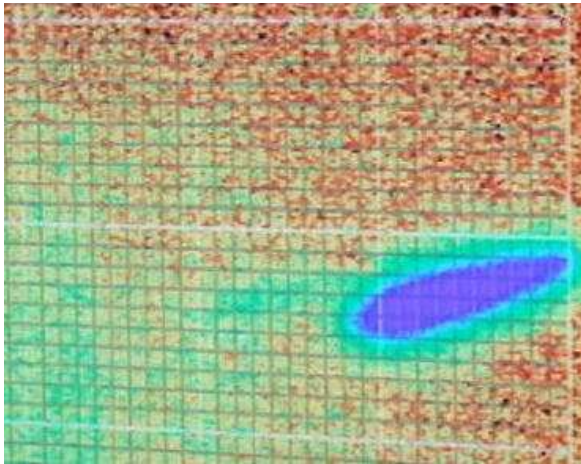
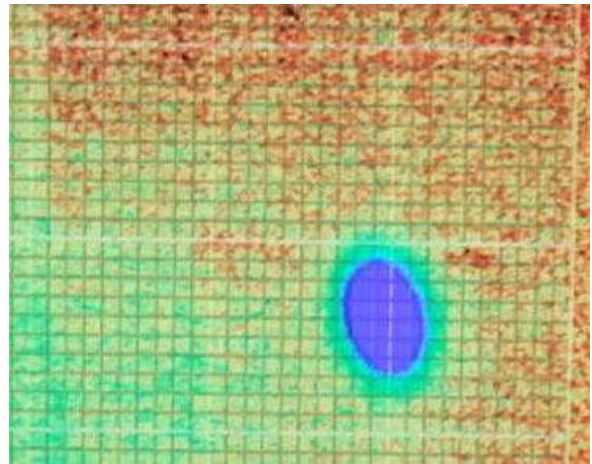


**Figure 19:** Results from  $x$ -scans for two different types of photomultipliers: (a) the  $2 \times 2$  MAPM (R7600U-03-M4, bias voltage 860 V), (b) the SAPM (R7400U-06, bias voltage 300 V). The absolute  $x$ -values correspond to different stage zero-positions; only the relative values are relevant.



(a) larger, elongated beam spot



(b) smaller, nearly round beam spot

**Figure 20:** Two beam spot shapes observed at ELSA when (a) the data in Fig. 19(a) and (b) the data in Fig. 19(b) were recorded. The dimensions of the spots are approximately  $4 \times 2$  mm for the elongated shape in (a) and  $1.5 \times 2$  mm for the rounder shape in (b).



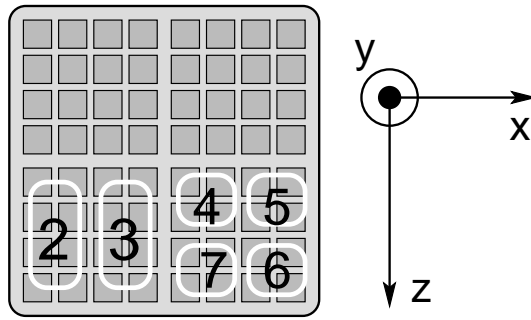


**Figure 21:** Readout configuration for the  $8 \times 8$  MAPM: The anode pads are depicted as grey squares; the readout channels as numbered white rectangles.

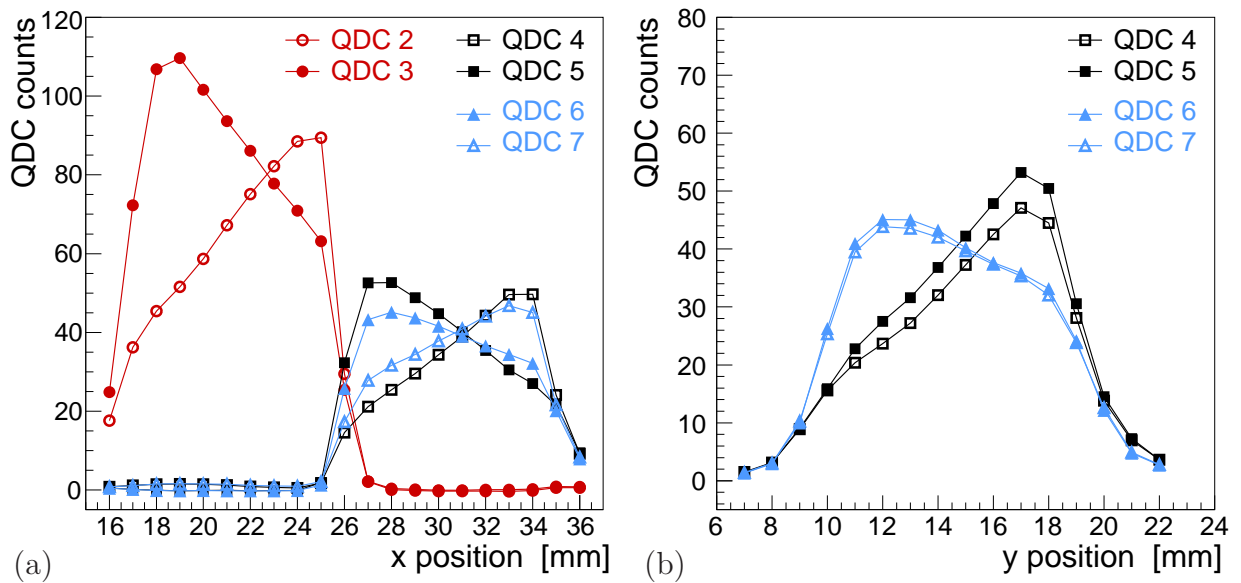


**Figure 22:** Beam position scan data recorded with the  $8 \times 8$  MAPM (bias voltage 500 V): (a) x-scan across both channels and (b) y-scan on the left channel.

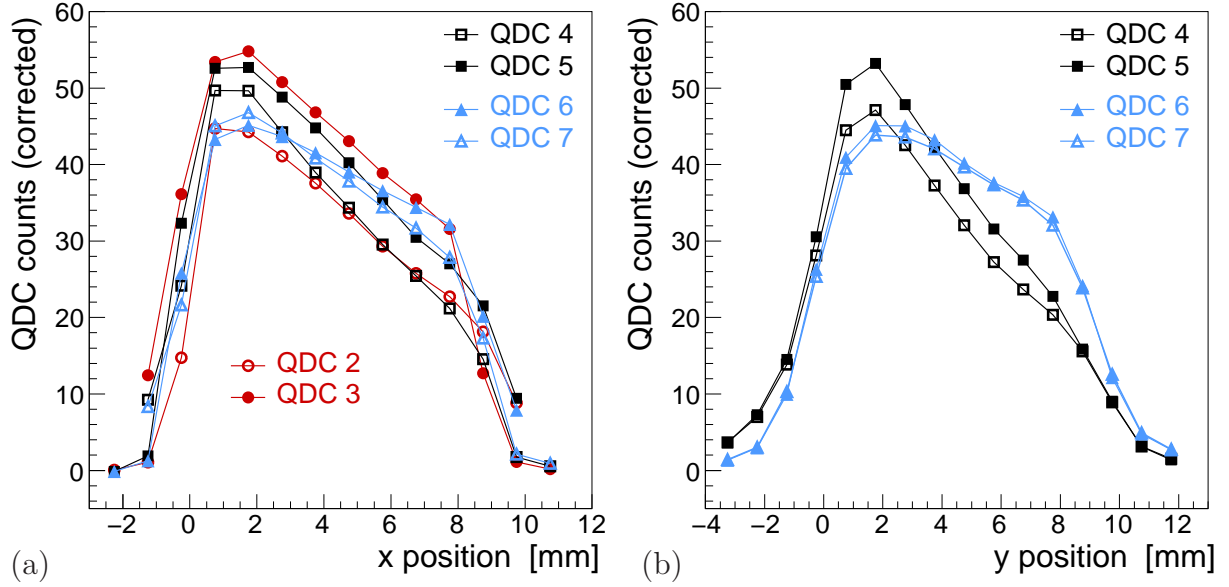


**Figure 23:** Different visualisation of the position scan data presented in Figure 22 with the emphasis on shape and amplitude differences: (a) x-scan data and (b) y-scan data.

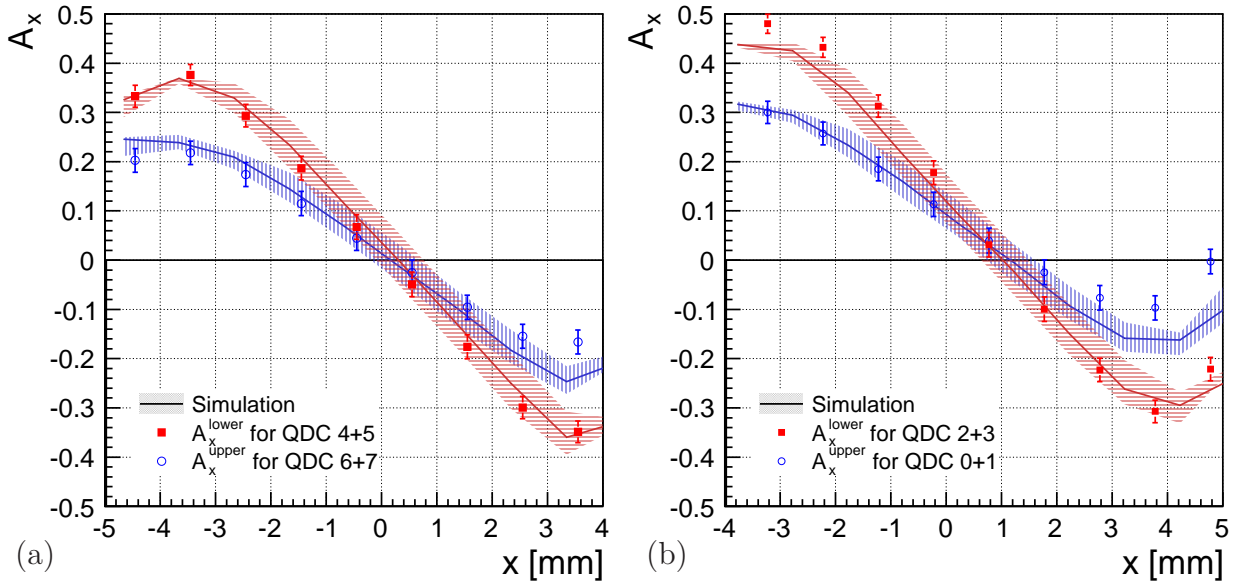


**Figure 24:** Asymmetries calculated from the position scan data sets recorded with the  $8 \times 8$  MAPM. (a)  $A_x$  for QDC-pairings 4+5 and 6+7 on the left detector channel from the same data as used in Fig 23 (b)  $A_x$  on the right detector channel from a subsequent run. In addition simulated asymmetries for  $\alpha_x = 0.2^\circ$  and  $\alpha_y = -0.2^\circ$  are shown for both channels. The error bands correspond to a variation of  $\alpha_y$  by  $\pm 0.1^\circ$ .